J. Fluid Mech. (1991), *vol.* 224, *pp.* 601–623
Printed in Great Britain

Microwave backscatter and acoustic radiation from breaking waves

By M. R. LOEWEN and W. K. MELVILLE

R. M. Parsons Laboratory, Massachusetts Institute of Technology, Cambridge, MA 02139, USA

(Received 21 February 1990 and in revised form 29 August 1990)

An experimental study of the microwave backscatter and acoustic radiation from breaking waves is reported. It is found that the averaged microwave and acoustic measurements correlate with the dynamics of wave breaking. Both the mean-square acoustic pressure and the backscattered microwave power correlate with the wave slope and dissipation, for waves of moderate slope ($S < 0.28$). The backscattered power and the mean-square pressure are also found to correlate strongly with each other. As the slope and wavelength of the breaking wave packet is increased, both the backscattered power and the mean-square pressure increase. It is found that a large portion of the backscattered microwave power precedes the onset of sound production and visible breaking. This indicates that the unsteadiness of the breaking process is important and that the geometry of the wave prior to breaking may dominate the backscattering. It is observed that the amount of acoustic energy radiated by an individual breaking wave scaled with the amount of mechanical energy dissipated during breaking. These laboratory results are compared to the field experiments of Farmer & Vagle (1988), Crowther (1989) and Jessup *et al.* (1990).

1. Introduction

This paper reports an experimental study of both the microwave backscatter and the sound produced by breaking waves in the laboratory. The study was motivated by the importance of wave breaking for the dynamics of the upper ocean, and the current lack of a reliable quantitative method of measuring active breaking in the field. One of the most common measures of breaking has been the whitecap coverage, which is defined as the fraction of the sea surface which is covered by whitecaps. It has been correlated with wind speed and atmospheric stability (Wu 1979; Monahan & O'Muirheartaigh 1986) but such correlations are indirect and subject to large uncertainties. Longuet-Higgins & Smith (1983) used a jump meter to measure the incidence of breaking in the field. The jump meter identified breaking by the amplitude of the time derivative of the surface elevation measured by a wave gauge mounted on a spar buoy.

Recent field experiments using microwave scatterometers (Jessup, Keller & Melville 1990) and passive acoustics (Crowther 1987, 1989; Farmer & Vagle 1987, 1988), have demonstrated that measurement of the statistics of breaking waves, and the identification of individual breaking events are possible using these remote sensing methods. Crowther (1987) observed that the fluctuations in the hydrophone signal, caused by breaking waves, could be as large as 20 dB. Farmer & Vagle (1988) found that the occurrence of a breaking wave above the sampling hydrophone could be detected by simply listening to the audio signal. Jessup *et al.* (1990) identified large events or 'sea spikes' in the time series of the radar cross-section and associated these with breaking waves. They showed that the contribution to the radar cross-section from sea spikes was approximately proportional to u_*^3, where u_* is the friction velocity. They also found that the contribution of an average sea spike to the radar cross-section was independent of u_*. Keller, Plant & Valenzuela (1981) correlated the Doppler spectra with breaking events and found that the scatterer speed during breaking increased and approached the phase speed of the dominant ocean waves. They also observed that the Doppler bandwidth was greatly increased during breaking. Ewell, Tuley & Horne (1984) tracked sea spikes at the sea surface, and found that they moved with a speed approximately equal to the phase speed of the dominant ocean waves.

There is considerable disagreement in the literature over which scattering mechanism produces the sea spikes. Alpers, Ross & Rufenach (1981) suggest that sea spikes are due to the spontaneous generation of Bragg waves at the steep crests of breaking waves. Kwoh & Lake (1981) studied the microwave backscatter from laboratory breaking waves and concluded that the backscatter could be separated into specular and non-specular components. The specular component was attributed to either the turbulent wake of the breaking wave or the capillary waves generated on the forward face of the steep wave. The non-specular component was attributed to wedge-like diffraction from the sharp-crested breaking wave, at or near breaking. Banner & Fooks (1985) made laboratory radar measurements of a quasi-steady stationary breaking wave. They found that the backscatter was due to Bragg scattering from the hydrodynamic disturbances, which were generated just downstream of the breaking crest.

Phillips (1988) used an approach which did not attempt to characterize the detailed scattering mechanism. He described the backscatter from breaking waves as the overall contribution from the family of surface configurations that are present throughout the breaking process. The contribution to the normalized radar cross-section from sea spikes and the frequency of occurrence of sea spikes are both predicted to be proportional to u_*^3.

Breaking waves are most probably the dominant source of high-frequency (>500 Hz) sea surface sound (Farmer & Vagle 1988). Many sound-generation mechanisms have been proposed: bubble bursting, bubble splitting and coalescence, collective bubble cloud oscillations and linear and nonlinear bubble oscillations (Kerman 1984; Prosperetti 1987; Banner & Cato 1987; Longuet-Higgins 1989). There is growing support for the theory that the most significant mechanism, at frequencies > 500 Hz, is bubble oscillation induced by the bubble formation process (Crowther 1989; Medwin 1989).

Farmer & Vagle (1988) conducted a field experiment using hydrophones to sample the sound produced by breaking ocean waves. They used a model of randomly distributed sound sources on the ocean surface to help them interpret the data. They found that an increase in the wind speed produced an increase in the mean distance between breakers and in the acoustic strength of individual breakers. They also noted that there is a competing effect when the wind speed increases: the wavelength increases, which tends to increase the mean breaker spacing, but the waves also become steeper, which tends to reduce the spacing. A peak in the acoustic spectra at twice the period of the dominant ocean waves was observed, which is consistent with the observation that waves tend to break at one-half the frequency of the dominant waves. This result is consistent with the fact that for deep water waves the phase velocity is twice the group velocity. In a recent field experiment Crowther (1989) observed that the sound sources under breaking waves moved at velocities

	P_1	P_2	P_3
Centre frequency f_c (Hz)	0.88	1.08	1.28
Theoretical break point x_b (m)	8.0	5.79	4.27
Centre component wavenumber k_c	3.56	4.92	6.68
Centre component phase speed c_c (m/s)	1.55	1.38	1.20

TABLE 1. Wave packet characteristics; $\Delta f/f_c = 0.73$ and $x_b k_c = 28.3$ for all wave packets.

approximately equal to one-half the wind speed, at an average speed less than that of the dominant ocean waves.

It is clear therefore that breaking waves are associated with large events in both the radar cross-section and the acoustic pressure, and that they can be identified in either of these time series. It may be that both measurement methods are well suited for the study of processes associated with wave breaking, including gas transfer, momentum transfer and energy dissipation at the air–sea interface.

Recently, Melville *et al.* (1988) presented results from some preliminary measurements of the microwave and acoustic signatures of laboratory breaking waves. They showed that the dissipation due to breaking correlated almost linearly with the backscattered microwave power and the mean-square acoustic pressure. The measurements were for one wave packet of centre frequency 0.88 Hz. These results were significant, because they showed, for the one wave packet studied, that dynamical information, such as the amount of energy dissipated due to breaking, could be inferred from the acoustic or microwave signal. To extend the measurements we have carried out simultaneous microwave, acoustic and surface displacement measurements of three wave packets of centre frequencies 0.88, 1.08 and 1.28 Hz. These frequencies correspond to wavelengths of 1.76, 1.28 and 0.94 m. We have also expanded the previous work by examining the duration of the hydrophone signal as a function of the acoustic and microwave signal levels, and by estimating the total acoustic energy radiated by the breaking events.

The processes of microwave scattering and acoustic radiation from breaking waves are clearly very complex. In this study we have attempted to avoid the complexities and first establish that the dynamics of breaking does indeed correlate with the simpler averaged microwave and acoustic measurements. Progress at this level would then justify a more detailed examination of the processes involved.

2. Experimental procedure

The experiments were conducted in a steel-framed glass wave channel 25 m long and 0.38 m wide at the R. M. Parsons Laboratory, MIT. The wave channel was filled with fresh water to a depth of 0.38 m for these experiments. A computer-controlled piston wave generator was programmed to focus a dispersive wave packet at a point x_b down the channel. The wave packets were synthesized from 32 sinusoidal components of constant slope ak, where a is the component amplitude and k is the component wavenumber. The components were equally spaced over a bandwidth, Δf, and centred at frequency, f_c. In these experiments three wave packets were used and their characteristics are listed in table 1.

It has been shown that deep-water breaking is a function of three dimensionless parameters: a bandwidth parameter $\Delta f/f_c$, a phase parameter $x_b k_c$ and a slope parameter S, where k_c is the centre component wavenumber, $S = Nak$ and N is the number of components (Melville & Rapp 1985; Rapp 1986). Experimental study showed that the dependence on $\Delta f/f_c$ and $x_b k_c$ was weak and that the dissipation due to wave breaking depended most strongly on the slope parameter S. In the present experiments, $\Delta f/f_c$ and $x_b k_c$ were held constant at 0.73 and 28.5 respectively, and S was varied.

The surface displacement was measured with a set of resistance-wire wave gauges which are described in detail by Rapp (1986). The surface displacement data was sampled at 100 Hz. The wave gauges were calibrated by sampling the still water level voltage for 8 s, as the gauge was moved in 2 cm increments from $+12$ to -10 cm. A third-order polynomial was fitted to the average voltage at each amplitude to give a calibration equation relating voltage to wave amplitude. The standard error of the fit of the equation to the data was calculated, and the calibration was accepted if the error was less than 0.04 cm.

Prior to each run the still water level was sampled for 20 s and subtracted from the measured data to remove any zero drift. Runs were separated by a minimum of 10 min to allow the surface oscillations in the channel to decay to negligible amplitudes. Rapp (1986) found that the variation in the linear term of the calibration equation was less than 1 % over 8 h. In order to minimize the errors due to variations in wave gauge calibration each wave gauge was calibrated every 4 h.

The acoustic measurements were made with an omnidirectional B & K model 8105 spherical hydrophone and a B & K 2635 charge amplifier. The frequency response of the hydrophone and amplifier system was constant to within ± 2 dB from 2 Hz to 20 kHz. The hydrophone signal was bandpass filtered from 500 Hz to 10 kHz and sampled at 20 kHz. The low-frequency cutoff at 500 Hz was used to remove the background noise of the wavemaker hydraulic system. The hydrophone was located vertically at mid-depth and transversely at the centre of the channel, mounted on an L-shaped bracket pointing upstream towards the breaking event. The bracket was supported from an overhead carriage which was set on rollers allowing the hydrophone to be moved easily along the channel. This configuration made it necessary to keep the hydrophone at least 2 m downstream of the breaking event to avoid vibrations caused by the surface waves striking the bracket during sampling.

Measurements of the sound produced by breaking waves in laboratory wave tanks may be difficult to interpret because of reverberation. If the wave tank is highly reverberant, absolute sound levels are difficult to measure because the sound is recorded more than once as it reflects back and forth past the hydrophone. We studied this problem in detail for our wave tank, and found that the sound measured was predominantly radiated away from the breaking region with negligible reflections from the endwalls of the tank. These results are discussed in §3.

The microwave backscatter was measured with a modified X-band CW Doppler radar manufactured by Kustom Electronics. The radar signal was bandpassed from 1–250 Hz and sampled at 500 Hz. The circularly polarized radar had a 15 cm aperture conical horn, was mounted 71 cm above the still water surface pointing in the upstream direction (looking into the advancing waves) at an incidence angle of 65°, and produced a 3 dB spot size of 1 m at the water surface. The far field of the aperture defined, by the criterion $R \geqslant 2d^2/\lambda$, is 1.53 m, where d is the diameter of the horn (Ulaby, Moore & Fung 1982). The centreline range was 1.68 m and the range variation over the 3 dB spot was 1.42 to 2.08 m to the still water surface.

The transmitted power of the radar was monitored during each run with a HP 432A power meter and a X486A temperature-compensated thermistor mount. There were no significant variations observed in the transmitted power. To avoid unwanted

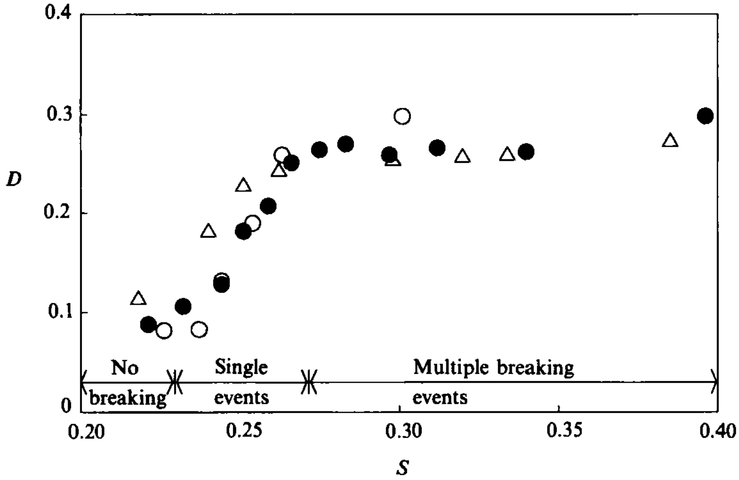

FIGURE 1. Fractional dissipation of wave packet energy as a function of the slope parameter S: ○, P_1; ●, P_2; △, P_3 (refer to table 1 for packet parameters). The variability of the data was typically less than the symbol size.

returns from the downward-pointing sidelobes of the radar, a panel of 40 dB radar absorbing material was placed beneath the horn. Absorbing material was also used to block reflections from the wave gauge mounting frame of the wave gauge placed upstream of the radar.

The linearity of the radar system was tested using a set of three metal spheres of diameters 15, 30 and 44 cm as targets. The spheres were suspended on nylon string from overhead and swung as pendulums to provide moving targets of known radar cross-section. The radar was mounted horizontally, aimed at the centreline of the spheres at the lowest point in their trajectories. Panels of radar absorbing material were mounted to cover the wave channel and shield each side of the swinging spheres to minimize the effect of multipath reflections. The procedure was based on the well-known equation for a monostatic radar,

$$P_r = \frac{P_t G^2 \lambda^2 \sigma}{(4\pi)^3 R^4}, \tag{1}$$

where P_r is the received power, P_t the transmitted power, G is the antenna gain and σ is the radar scattering cross-section (Ulaby *et al.* 1982). In this case P_t, G and λ are constants and therefore $\log P_r = \log(\sigma/R^4) + \text{constant}$. We varied the range R from 2 to 16 m and the radar cross-section σ had three values, 0.018, 0.073 and 0.16 m^2, corresponding to the areas of the three metal spheres.

At each value of R and σ, three runs were performed by swinging the spheres and sampling the data on a HP 3561A signal analyser. The returned power was taken as the average over the three runs. The data followed the radar equation with maximum errors of ± 2 dB, demonstrating that the radar system was linear. At larger ranges multipath reflections could not be avoided because it became impractical to shield a large enough area of the laboratory with absorbing material. The data followed the radar equation for received voltage amplitudes from 20 mV to 320 mV. The lower limit was imposed by multipath reflections at larger ranges and the upper limit was imposed owing to the practical limit on the radar cross-section (i.e. larger spheres than the 44.4 cm diameter one used were not practical within our laboratory set-up). At larger voltage amplitudes (up to 4 V) the radar frequency response was found to be uniform from 1 Hz to 2 kHz. The backscattered radar signals, during the breaking experiments, were typically in the range ± 2 V and the largest voltage amplitudes observed were 4 V. Therefore, we concluded that the radar behaviour was linear over the range of signal amplitudes observed during the experiments.

3. Results

3.1. *Wave dissipation*

The surface displacement was measured with an array of resistance-wire wave gauges, positioned upstream and downstream of the breaking event. Rapp & Melville (1990) have demonstrated that when the surface displacement variance is used to estimate the momentum flux of weakly nonlinear, slowly varying, two-dimensional, deep-water waves, errors of the order of 5% are incurred. We would expect errors of similar magnitude in these experiments because our wave packet parameters are very similar to theirs. The centre frequencies and bandwidths were the same but in our work the water depth was 0.38 m compared to their depth of 0.6 m. The surface displacement variance $\overline{\eta^2}$ is given by

$$\overline{\eta^2} = \frac{1}{T}\int_0^T \eta^2(t)\,\mathrm{d}t, \tag{2}$$

where $\eta(t)$ is the surface displacement and T is the length of the sampling interval. The fractional dissipation D due to breaking is given by

$$D = \frac{\overline{\eta_\mathrm{d}^2}}{\overline{\eta_0^2}} \equiv \left(\frac{\overline{\eta_0^2}-\overline{\eta_\mathrm{f}^2}}{\overline{\eta_0^2}}\right), \tag{3}$$

where $\overline{\eta_0^2}$ and $\overline{\eta_\mathrm{f}^2}$ are the surface displacement variances upstream and downstream of the event. Figure 1 shows the dissipation D as a function of the wave slope parameter S. The data collapse onto a single curve similar to the data presented by Melville & Rapp (1985). There is a threshold at $S = 0.23$, below which no breaking occurs. In the range, $S = 0.23$–0.28, the dissipation increases rapidly, reaching a plateau at $D \approx 0.30$, and then remains approximately constant for $S > 0.28$. For values of $S < 0.23$ the dissipation is approximately constant at 0.10, consistent with theoretically predicted losses due to viscous dissipation (Rapp 1986).

3.2. *Microwave scattering*

A typical radar time series and the corresponding Doppler spectrum are shown in figure 2. The breaking events were found to be associated with the higher frequency components of the signal, which in figure 2(*a*) occur in the interval 2.5–3.2 s. The spectrum in figure 2(*b*) has a well-defined minimum at 50 Hz which was typical for all events observed.

In figure 3 a set of radar spectra, for time series bandpass filtered from 1–250 Hz and sampled at different locations along the channel are shown. In figure 3 the spectra at 9.5, 10 and 10.5 m have considerable energy above the ambient levels for frequencies < 50 Hz. This energy is not associated with the breaking wave because it was also observed at these locations for lower amplitude non-breaking waves. Similar behaviour was observed for the two other wave packets as well, which led us to conclude that for the wave frequencies used in these experiments, the

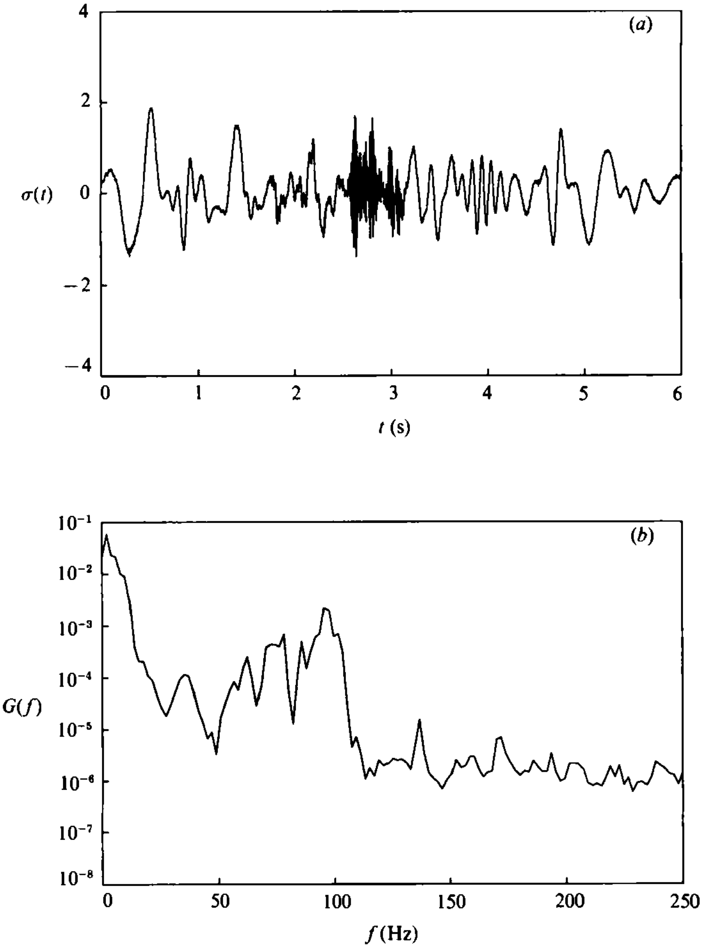

FIGURE 2. (*a*) Time series of radar signal bandpass filtered from 1–250 Hz, for P_1 with $S = 0.254$. (*b*) Power spectrum of time series in (*a*).

backscattered microwave power due to breaking corresponded to frequencies in the range 50–250 Hz. The energy below 50 Hz is likely due to the backscatter from the orbital motions of the waves or from capillary waves near the crest of steep but unbroken waves.

In figure 4(*a*) a set of radar time series, bandpass filtered from 50–250 Hz and a matching hydrophone time series, bandpass filtered from 500–10000 Hz, are displayed. In figure 4(*b*) a series of photographs, matching the radar and acoustic time series of figure 4(*a*), show the evolution of a breaking wave with time.† The mean water surface elevation is marked by the horizontal tape and the tick marks denote 0.5 m intervals. The centreline of the radar antenna pattern is marked by the angled tape above the mean water level. In figure 4(*b*), photograph (i) ($x = 8$ m, $t = 1.12$ s), the unbroken wave crest is downstream of the radar centreline, there is no

---

† The data in figure 4(*a*) and the photographs in figure 4(*b*) were taken with a water depth of 0.364 m compared to 0.38 m which was used for the bulk of the experiments. This was necessary because at a depth of 0.38 m the wave crest was hidden from view behind the upper steel beam of the wave tank. We observed no significant differences between the radar and acoustic signals at the two depths.

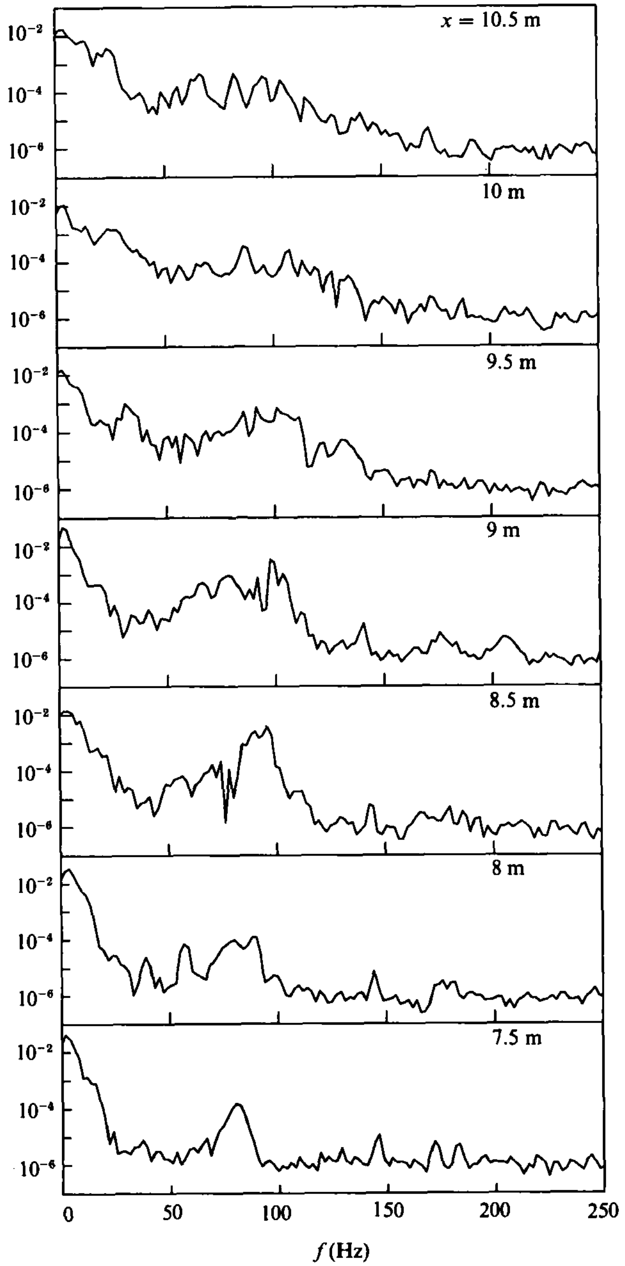

FIGURE 3. Radar Doppler spectra at various x-locations for P_1 with $S = 0.254$, radar time series were bandpass filtered from 1–250 Hz.

acoustic signal and the amplitude of the radar signal is very small. In (ii) ($x = 8.5$ m, $t = 1.2$ s) the unbroken crest is slightly downstream of the radar centreline, there is still no acoustic signal and the radar signal amplitude is large. The large backscattered signal is probably due to specular reflection from the steep forward face of the wave which is located just downstream of the centre of the beam but still within the 3 dB beamwidth. The wave is still unbroken and no sound has been produced in (iii) ($x = 9$ m, $t = 1.32$ s), the steep forward face of the wave is directly

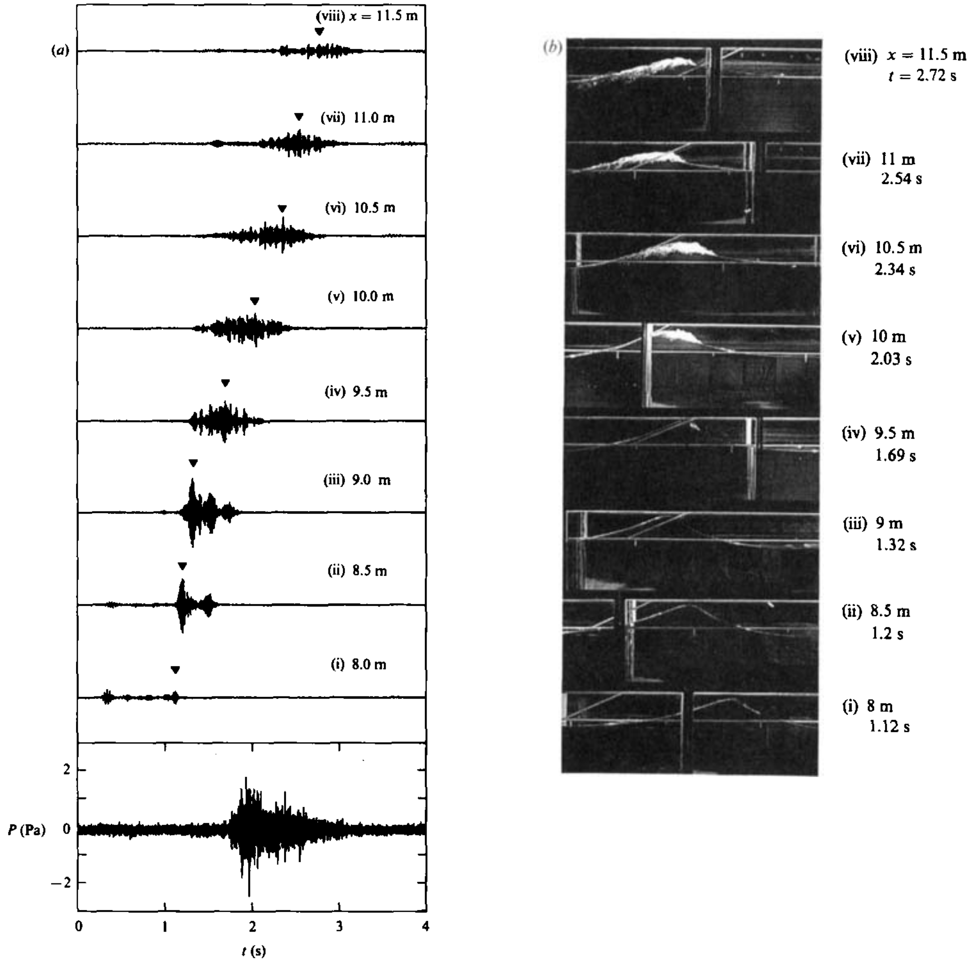

FIGURE 4. (*a*) Bottom trace is a hydrophone time series bandpass filtered in the range 500 Hz–10 kHz, upper traces are radar time series at various x-locations, bandpass filtered in the range 50–250 Hz, for P_1 with $S = 0.254$. (*b*) Photographs of a breaking wave matching the data in (*a*). Each photograph corresponds to one radar time series and the time the photograph was taken is marked in (*a*) with a ▼ above the matching radar time series.

in line with the centreline of the radar beam and the radar signal amplitude is at a maximum. The beginning of sound production coincides with (iv) ($x = 9.5$ m, $t = 1.69$ s), the wave has begun to break, the crest is in line with the centre of the radar beam and the radar signal amplitude has begun to decrease. The wave is breaking vigorously in (v) ($x = 10$ m, $t = 2.03$ s) and the acoustic signal amplitude is large. In photographs (vi), (vii) and (viii) the wave is actively breaking and both the radar and acoustic signal amplitudes are decreasing with time. In (vii) the crest is at the centreline of the radar beam, the acoustic signal amplitude has decreased to 50% of the maximum and the radar signal amplitude is 35% of its maximum.

These photographs and time series clearly show that a large portion of the backscattered microwave power associated with breaking is due to scattering from the steep forward face of the wave prior to the start of active breaking and sound generation. They also show that the majority of the sound energy produced by breaking occurs during the early stages of active breaking, see figure 4(*b*)(v). In the

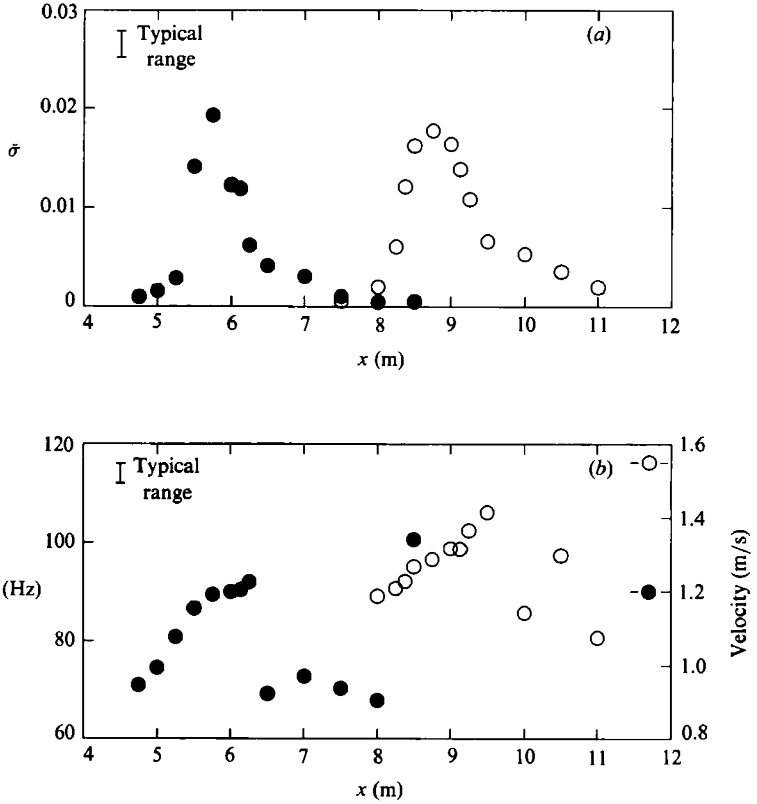

FIGURE 5. (*a*) Time-averaged radar cross-section as a function of x. (*b*) Peak frequency (Hz) of the radar Doppler spectrum as a function of x. ○, P_1, $S = 0.254$; ●, P_3, $S = 0.385$; —○— and —●— on (*b*) denote the centre component phase speeds for P_1 and P_3 respectively. Each datapoint is averaged from 3 runs at each location; radar data were bandpass filtered in the range 50–250 Hz. The typical variability of the data between runs is shown by the scatter bars.

latter stages, figure 4(*b*)(vii) and (viii), the bubble cloud is still clearly visible but sound amplitudes have decreased significantly.

The more energetic breaking events covered an area larger than the area illuminated by the radar. In order to obtain a single measure of the backscattered power from each event and to eliminate the influence of the antenna, it was necessary to take radar measurements at a number of positions along the channel. At each location the time-averaged radar cross-section $\bar{\sigma}(x)$ was calculated from

$$\bar{\sigma}(x) = \frac{1}{T}\int_0^T \tilde{\sigma}(x,t)\,\mathrm{d}t, \qquad (4)$$

where T is the length of the sample and $\tilde{\sigma}(x,t)$ is the time series of the radar cross-section as a function of both x and t. Two examples of the time-averaged radar cross-section as a function of position along the channel are shown in figure 5(*a*). Both events shown are typical, with $\bar{\sigma}(x)$ increasing from zero to a well-defined peak and then decaying towards zero as x increases.

The peak frequency is defined as the frequency of the maximum value of the Doppler spectrum. It is a measure of the velocity of the dominant scatterers present in the illuminated area during the sampling interval. In figure 5(*b*) the peak frequency, corresponding to the data in figure 5(*a*), is plotted. It was calculated from

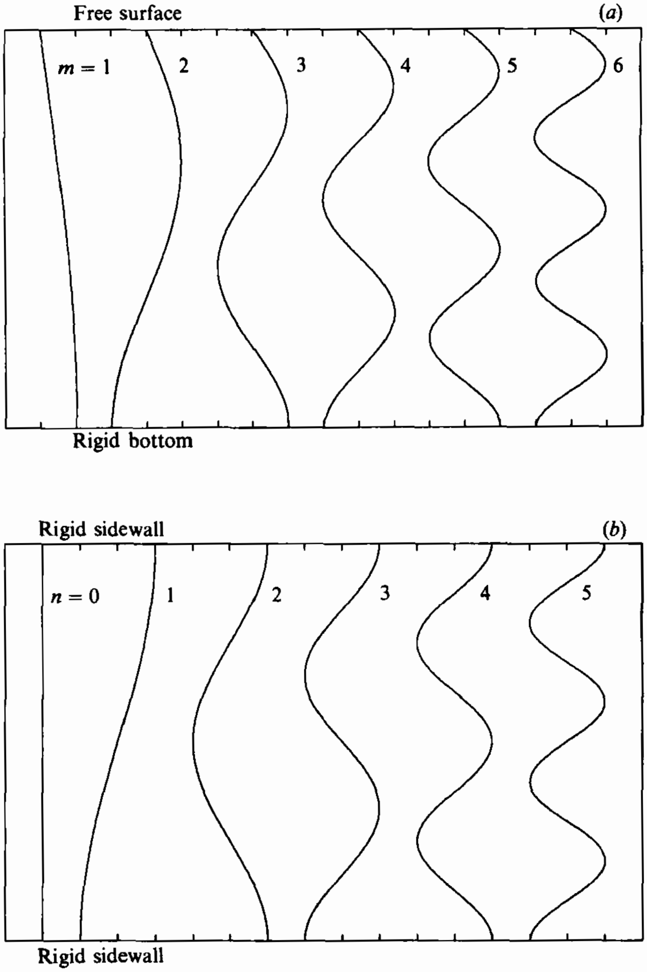

FIGURE 6. (*a*) Vertical eigenfunction shapes; *m* is the vertical mode number. (*b*) Horizontal eigenfunction shapes; *n* is the horizontal mode number.

the Doppler spectrum of the radar signal bandpassed from 50–250 Hz. The maximum peak frequencies for the two events plotted in figure 5(*b*) are close to the phase velocities of the centre components for their respective wave packets, see table 1.

3.3. *Acoustic radiation*

The acoustic field is dominated by the modal structure present in the wave tank. If the tank sidewalls and bottom are assumed to be rigid and the free surface to be a pressure release surface the mode shapes are given by

$$\varphi_m^{\mathrm{v}}(z) = \sin\left(\frac{(2m-1)\,\pi z}{2H}\right), \quad m = 1, 2, \ldots, \infty, \tag{5}$$

$$\varphi_n^{\mathrm{h}}(y) = \cos\left(\frac{n\pi y}{W}\right), \quad n = 0, 1, \ldots, \infty, \tag{6}$$

where $\varphi_m^{\mathrm{v}}(z)$ is the vertical eigenfunction, z is the vertical coordinate, H is the water

Horizontal mode number n	Vertical mode number m	Theoretical cutoff frequency (Hz)
0	1	990
0	2	2960
0	3	4930
0	4	6910
0	5	8880
1	1	2210
1	2	3560
1	3	5310
1	4	7190
1	5	9100
2	1	4070
2	2	4940
2	3	6320
2	4	7960
2	5	9720
3	1	6010
3	2	6630
3	3	7710
3	4	9100
4	1	7960
4	2	8430
4	3	9310
5	1	9920

TABLE 2. Acoustic modes and their theoretical cutoff frequencies.

depth, $\varphi_n^{\mathrm{h}}(y)$ is the horizontal eigenfunction, y is the transverse coordinate and W is the tank width (Brekhovskikh & Lysanov 1982). The mode shapes are composed of combinations of one horizontal and one vertical eigenfunction. The first six vertical and horizontal eigenfunctions are illustrated in figure 6. The cutoff frequencies of the modes are given by

$$F_{\mathrm{c}} = \frac{c}{2\pi}(k_z^2 + k_y^2)^{\frac{1}{2}} \tag{7}$$

where F_{c} is the cutoff frequency in Hz, k_z is the vertical wavenumber and k_y is the transverse number. In table 2 the modes with cutoff frequencies less than 10 kHz are listed.

A typical acoustic spectrum for a breaking wave and the spectrum of the background noise are shown in figure 7. There is energy above the background levels across the entire spectrum, but most of the energy is between 2200 and 4500 Hz. The cutoff at 2200 Hz is most prominent and was clearly evident in the spectra of all events. It is not clear why the lowest-order mode with $m = 1, n = 0$ and a cutoff frequency of 990 Hz is not observed.

We investigated the influence of reverberation on the acoustic measurements. Two hydrophones were positioned at mid-depth in the tank, several metres downstream of the breaking location, separated by a distance Δx in the longitudinal direction. The acoustic signal from a breaking wave was then recorded simultaneously using both hydrophones and the phase and time delay between them was calculated.

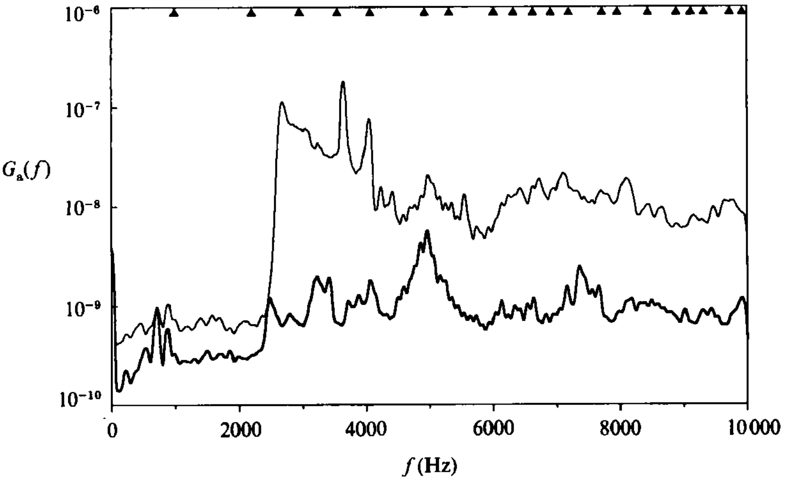

FIGURE 7. Upper curve: acoustic spectrum for P_1 with $S = 0.254$; lower curve: the spectrum of the background noise. ▲, Location of cutoff frequencies.

In figure 8 the coherence, $\gamma^2_{xy}(f)$, and the phase spectrum, $\theta_{xy}(f)$, for a run with $S = 0.263$ and $\Delta x = 1.15$ m are shown. The coherence is defined by

$$\gamma^2_{xy}(f) = \frac{|G_{xy}(f)|^2}{G_{xx}(f)\,G_{yy}(f)}, \tag{8}$$

where $G_{xy}(f)$ is the cross-spectral density function of the two time series $x(t)$ and $y(t)$, $G_{xx}(f)$ and $G_{yy}(f)$ are the autospectral density functions of $x(t)$ and $y(t)$ respectively. The phase spectrum is given by

$$\theta_{xy}(f) = \tan^{-1}\frac{Q_{xy}(f)}{C_{xy}(f)}, \tag{9}$$

where $Q_{xy}(f)$, the quad-spectrum, and $C_{xy}(f)$, the co-spectrum, are defined by

$$G_{xy}(f) = C_{xy}(f) - jQ_{xy}(f) \tag{10}$$

(Bendat & Piersol 1986). From figure 8 it is seen that where the coherence is high the phase spectrum is ordered and continuous. The positive slope of $\theta_{xy}(f)$ indicates that $y(t)$, which corresponds to the hydrophone closest to the event, leads $x(t)$, consistent with the acoustic energy propagating downstream away from the breaking location.

The data from the pair of hydrophones were digitally processed to obtain the time delay between the two signals. The processing consisted of bandpassing the two signals in a narrow band over which the coherence was high and then rectifying and lowpassing to obtain the envelopes of the two signals. The two envelopes were then cross-correlated and the time delay found by locating the maximum in the cross-correlation sequence. Using the time delay and the distance Δx between the two hydrophones the group velocity was calculated. The group velocities for the modes of the wave tank can be computed using the following equation:

$$C_g = C(1.0 - (F_c/f)^2)^{0.5}, \tag{11}$$

where C_g is the group velocity, C the phase speed, F_c the cutoff frequency (cf. equation (7)) and f the frequency (Brekhovskikh & Lysanov 1982). In figure 9 the

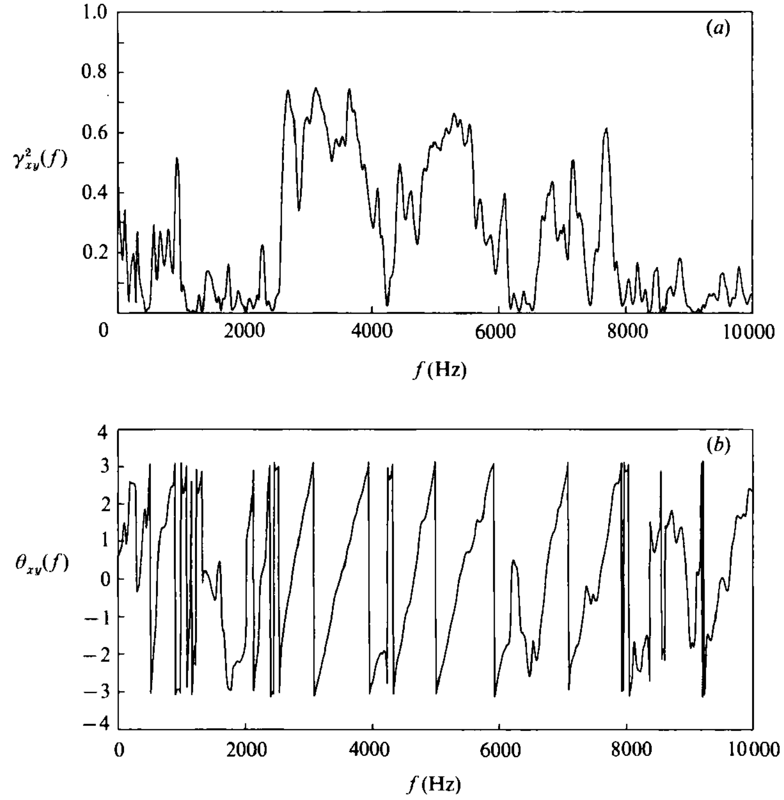

FIGURE 8. (*a*) Coherence $\gamma^2_{xy}(f)$; (*b*) phase spectrum $\theta_{xy}(f)$ of two hydrophone signals. $S = 0.263$ and separation distance $\Delta x = 1.15$ m.

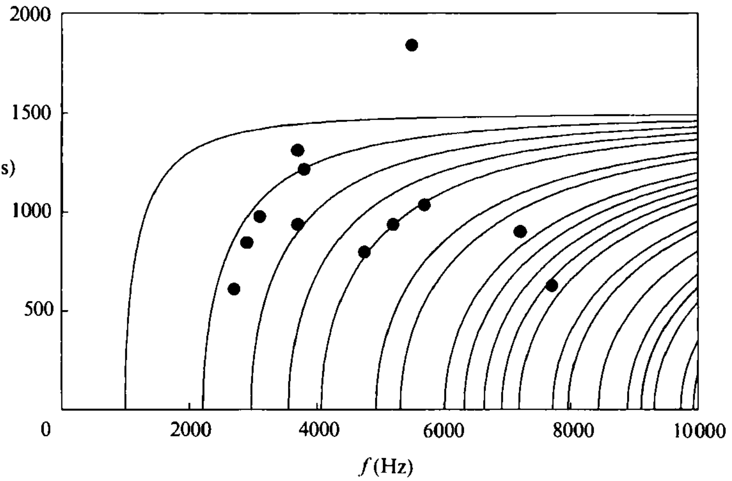

FIGURE 9. Solid curves show equation (11), the theoretical values for the group velocities of the acoustic modes in the wave channel; ●, estimates of the group velocities from the time delay processing.

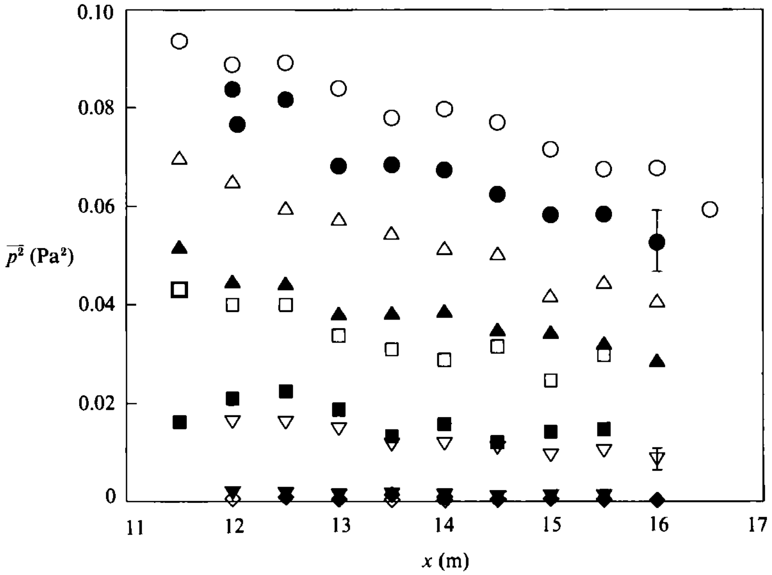

FIGURE 10. Mean-square acoustic pressure as a function of x. All data are for P_1: ○, $S = 0.286$; ●, $S = 0.274$; △, $S = 0.263$; ▲, $S = 0.254$; □, $S = 0.249$; ■, $S = 0.247$; ▽, $S = 0.244$; ▼, $S = 0.241$; ◇, $S = 0.237$; ◆, $S = 0.226$. Each data point is the average of 5 runs and the typical variability of the data between runs is shown by the scatter bars. The scatter becomes smaller as S decreases.

theoretical curves given by (11) and the group velocities obtained from the time delay estimates are compared. Except for the one outlier at 5500 Hz the agreement is good and the time delays obtained showed that the signal from the hydrophone closer to the breaking event leads the other signal as expected. The data points estimated using the time delay technique were at frequencies where the two signals were significantly correlated, that is had a coherence exceeding 0.5.

To study the acoustic attenuation along the channel, hydrophone measurements were taken at a number of positions downstream of the breaking event. Figure 10 shows a set of data from our earlier experiments, which were reported in Melville *et al.* (1988), showing the attenuation of the mean-square acoustic pressure, $\overline{p^2}(x)$, where

$$\overline{p^2}(x) = \frac{1}{T}\int_0^T p(x,t)^2\,\mathrm{d}t, \tag{12}$$

where $p(x,t)$ is the acoustic pressure, and T is the duration of the sampling interval. The attenuation rate is approximately constant for a given slope, S, and at a given x-location the mean-square pressure increases with increasing S. In the present study hydrophone measurements were taken over a range of 4 m in the x-direction for one third of the events, and over a range of 2 m for the remaining events. Extrapolating over twice the distance from the sampling location of the hydrophone to the wavemaker paddle or to the endwall showed that the sound had decayed to negligible levels before returning to the hydrophone location.

The results for the attenuation of the acoustic signal along the tank, the slope of the phase spectrum and the sign and magnitude of the group velocity all demonstrate that the acoustic measurements were not corrupted significantly by reflections or excessive reverberation. The relative phase of the two signals at frequencies at which the coherence is high and the time delay estimates for the entire signals confirm that the acoustic energy was propagating away from the breaking location.

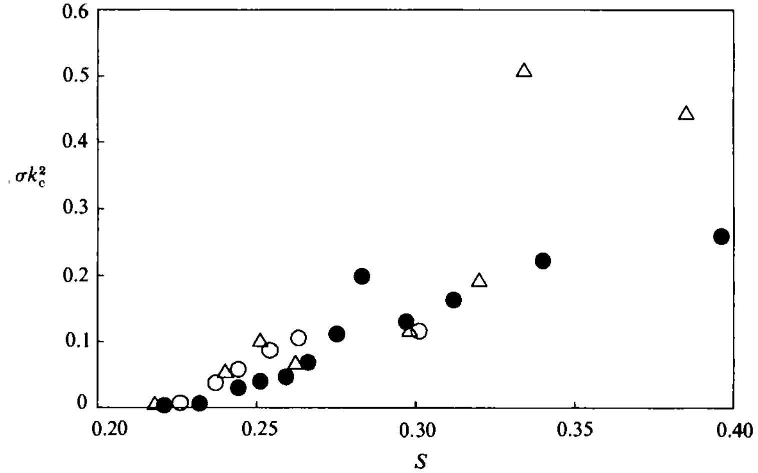

FIGURE 11. Dimensionless radar cross-section σk_c^2 as a function of the slope parameter S: ○, P_1; ●, P_2; △, P_3.

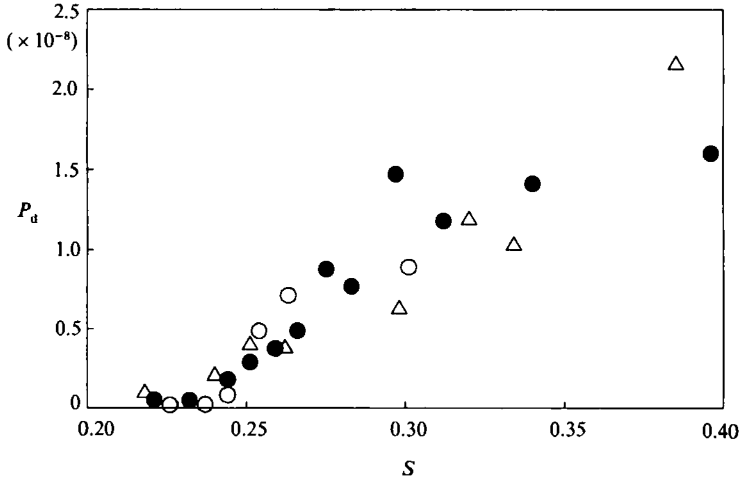

FIGURE 12. Dimensionless mean-square acoustic pressure P_d as a function of the slope parameter, S: ○, P_1; ●, P_2; △, P_3.

3.4. *Empirical scaling and correlations*

A single measure of the backscattered microwave power was obtained by integrating the time-averaged radar cross-section $\bar{\sigma}(x)$, along the channel in x. Defining the radar cross-section as

$$\sigma = \frac{1}{L_e}\int_0^{L_e} \bar{\sigma}(x)\,\mathrm{d}x, \tag{13}$$

where L_e is the length of the longest event measured, T is the sampling time and $\bar{\sigma}(x)$ is the time-averaged radar cross-section. The radar cross-section has units of length squared and is most naturally scaled by the wave packet centre component wavenumber, k_c. In figure 11 the scaled radar cross-section, σk_c^2, is plotted as a function of the slope parameter, S. The data collapse onto a single curve and there

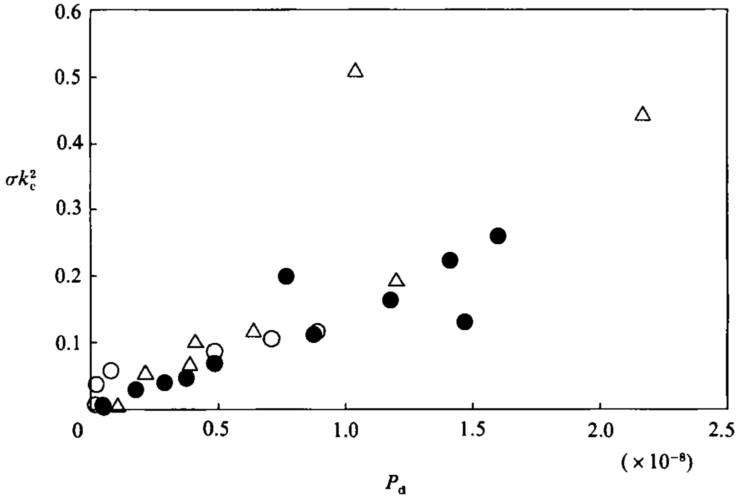

FIGURE 13. Correlation between the dimensionless radar cross-section σk_c^2 and the dimensionless means square acoustic pressure P_d: ○, P$_1$; ●, P$_2$; △, P$_3$.

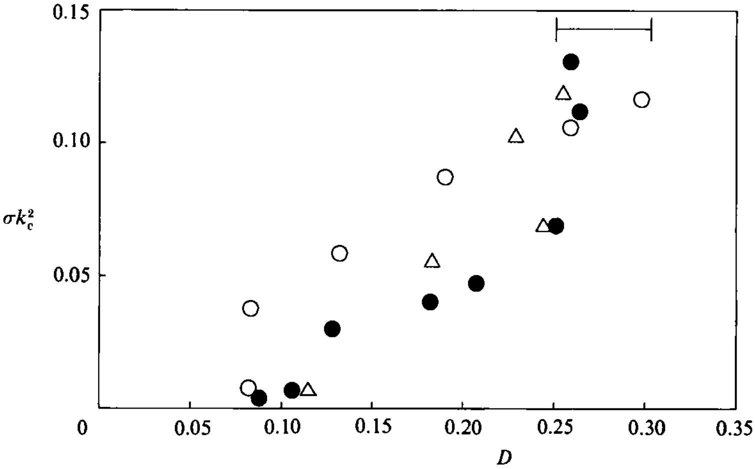

FIGURE 14. Correlation of the dimensionless radar cross-section σk_c^2 with the fractional dissipation D. For $\sigma k_c^2 > 0.15$ the data are independent of D and fall within the range marked |——|. ○, P$_1$; ●, P$_2$; △, P$_3$.

is a linear correlation between the dimensionless radar cross-section and the wave slope.

A dimensionless mean-square pressure can be defined by scaling with $(\rho c_c^2)^2$,

$$P_d = \frac{\overline{p^2}(x)}{(\rho c_c^2)^2} \tag{14}$$

where ρ is the density of water and c_c is the phase speed of the centre frequency component. We chose to use $\overline{p^2}(x)$ measured 7 m downstream from the breaking location in calculating P_d. In figure 12 the dimensionless mean-square pressure, P_d, is shown as a function of the slope parameter, S. The data falls onto a single curve and a linear correlation is again evident.

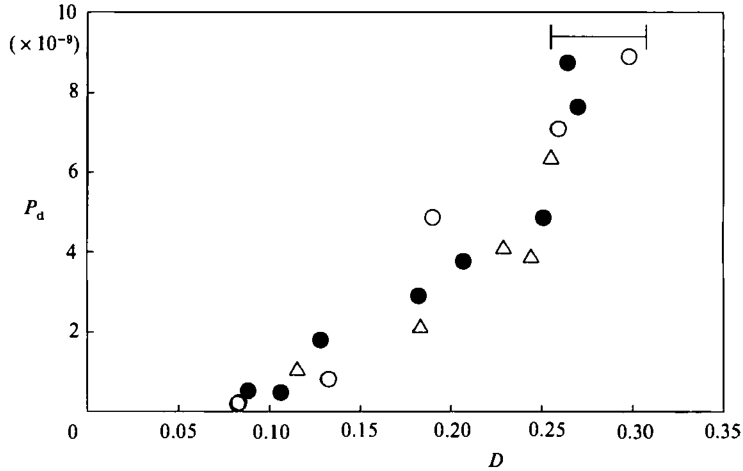

FIGURE 15. Correlation of the dimensionless mean-square acoustic pressure P_d with the fractional dissipation D. For $P_d > 10^{-8}$ the data are independent of D and fall within the range marked |——|. ○, P_1; ●, P_2; △, P_3.

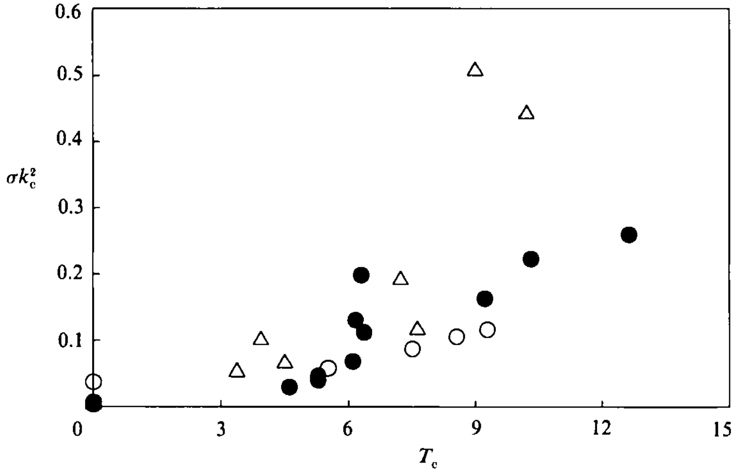

FIGURE 16. Correlation of the dimensionless radar cross-section σk_c^2 and the dimensionless hydrophone signal duration T_c. ○, P_1; ●, P_2; △, P_3.

It was of interest to see if the radar and hydrophone signals were correlated. The dimensionless radar cross-section, σk_c^2, and the dimensionless mean-square pressure, P_d, are plotted in figure 13. A strong correlation is evident except for one outlying point which remains unexplained. The experimental data for this outlier at $P_d = 10^{-8}$ and $\sigma k_c^2 = 0.5$ have been verified by repeating the complete experimental run for this data point.

The microwave and acoustic signals were observed to correlate with the dissipation. In figure 14 the dimensionless radar cross-section is plotted as a function of dissipation. It increases linearly as D varies from 0.10 to 0.25 and is independent of D for $\sigma k_c^2 > 0.15$, with the data falling between 0.25 and 0.30. The dimensionless mean-square pressure is plotted as a function of D in figure 15, it increases linearly as D increases from 0.10 to 0.25 and it is independent of D for $P_d > 10^{-8}$, with the data falling between 0.25 and 0.30.

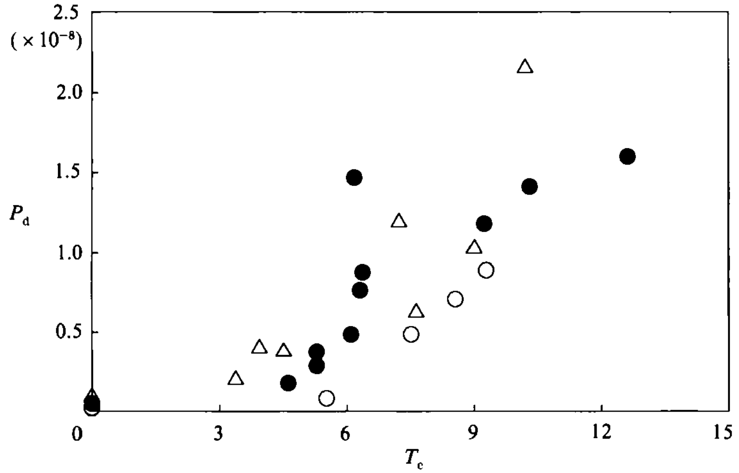

FIGURE 17. Correlation of the dimensionless mean-square acoustic pressure P_d and the dimensionless hydrophone signal duration T_c. ○, P_1; ●, P_2; △, P_3.

The duration of the hydrophone signal was measured by visually determining the beginning and end of sound production from the acoustic time series. The measurements were converted to a dimensionless timescale, T_c, by multiplying by the radian frequency of the centre component of the wave packet. The correlations of the radar cross-section and the mean-square pressure with the duration are shown in figures 16 and 17. There is some scatter in the data but, with the exception of one or two outlying points, the dimensionless radar cross-section and the dimensionless mean-square pressure are approximately proportional to the dimensionless duration.

4. Discussion

The results presented above show that the backscattered microwave power and the radiated acoustic energy correlate with the wave slope and the energy dissipation due to breaking over a range of wave parameters. The correlation is strongest at wave slopes within the range commonly observed in ocean waves, $S < 0.30$. We also found that the backscattered microwave power and the radiated acoustic energy were correlated.

The observation that a large portion of the backscattered microwave power precedes the onset of sound production and visible breaking has several implications. One is that the backscatter from breaking is strongly influenced by the geometry of the wave prior to breaking. If, following Phillips (1988), we consider the backscatter as the overall contribution from the family of surface configurations present during breaking, we note that the configurations occurring just prior to breaking may be the dominant ones. Another implication is that the unsteadiness of the breaking process is important and therefore the large cross-sections we measured prior to impact would not be observed in quasi-steady breaking (cf. Banner & Fooks 1985).

During breaking we observed that the peak frequency of the Doppler spectrum increased and approached a value corresponding to a velocity within 10% of the phase speed of the centre component of the wave packet. Field observations have shown that the speed of the scatterers during breaking approaches that of the phase speed of the dominant ocean waves and this is consistent with our results (Keller

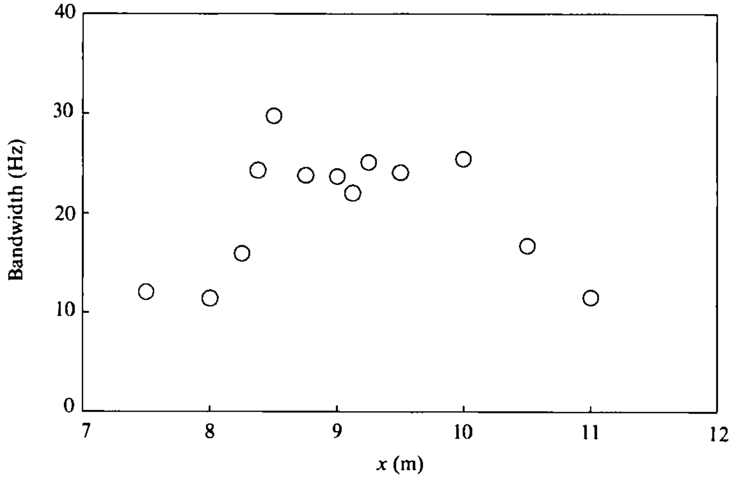

FIGURE 18. Variation of the bandwidth with x, the distance along the tank. ○, P_1, $S = 0.254$. Data correspond to the spectra in figure 3.

et al. 1981; Ewell *et al.* 1984). Keller *et al.* (1981) also reported that the bandwidth of the Doppler spectrum was drastically increased by breaking and that it could easily be increased by a factor of as much as 2.

The bandwidth of the Doppler spectrum, B, is defined as the square root of the second central moment, and is given by

$$B = \left\{ \int_0^{+\infty} (f-\bar{f})^2 G(f)\,\mathrm{d}f \right\}^{\frac{1}{2}}, \tag{15}$$

where f is the frequency, $\bar{f}$ is the centroid frequency and $G(f)$ is the magnitude of the radar Doppler spectrum. The bandwidth for the event with $S = 0.254$, matching the spectra shown in figure 3, is plotted in figure 18. We see that the bandwidth is 10 Hz at locations where the backscattered power is negligible (7.5, 8 and 11 m) and is increased by a factor of 2.5 to 25 Hz at the locations of large backscattered power. These results are consistent with the field observations of Keller *et al.* (1981).

Our results show that the backscattered microwave power and the radiated acoustic energy both increase as wave slope and wavelength are increased. This is consistent with Phillips' (1988) hypothesis that the radar return from longer waves should be more intense. It is also consistent with Farmer & Vagle's (1988) result, which showed that the acoustic strength of individual breakers increased with wind speed. Jessup *et al.* (1990) found that the average radar cross-section of an individual sea spike may be independent of the friction velocity, u_*. This result is difficult to compare to our laboratory measurements because the relationship between u_* and our wave slope parameter is complicated. The dominant wave slope in the field is a function of both u_* and the wave age defined by u_*/c, where c is the phase speed of the waves.

In Jessup *et al.* (1990) the radar spot was approximately 2 m in size and the typical dominant surface wavelength was 50 m. It may be that the sea spikes they observe in the field are due to specular reflection as the local wave slope within the illumination area becomes sufficiently steep. If this is the case once the surface waves are sufficiently long and steep to create an area as large as the radar spot, the signal may saturate, and further increases in wave slope or wavelength would not increase the power returned in an individual sea spike. In our laboratory experiments the radar spot size was approximately 1 m and typical surface wavelengths were 1.5 m. Therefore our results are not affected by saturation of the backscattered signal and we observe a strong dependence on both wave slope and wavelength.

The experiments were conducted in fresh water and this raises the issue of how applicable our results are to remote sensing of the ocean. The major difference between fresh water and sea water breaking waves is that the bubbles generated in sea water persist longer (Medwin & Daniel 1990). This has a minimal effect on the microwave signal because we observed that the geometry of the prebreaking wave dominates and that the duration of the backscattered signal is of the order of the wave period. Medwin & Daniel (1990) have found that the sound radiated by small-scale spilling breakers in fresh water and sea water is essentially the same. They state that the issue of bubble persistence is not important because the sound generated by breaking waves is from pulsating bubbles which radiate sound for only a few milliseconds after they are formed at the surface. We conclude that the differences between fresh and salt water breaking waves are unimportant for these types of measurements and that the results presented here should apply to remote sensing of the ocean surface.

The acoustic energy radiated by a breaking wave can be estimated using the following equation:

$$E_{\mathrm{a}} = \frac{\overline{p^2}}{\rho c} A m T_{\mathrm{p}}, \tag{16}$$

where T_{p} is the sampling interval and m is a factor used to account for the modal structure in the wave channel. We kept the sampling hydrophone at the centre of the channel cross-section for our experiments, so we had a point measurement of the acoustic pressure at each x-location. The modal factor m was used to compensate for the fact that the mean-square pressure may not be constant across the channel. To obtain m, experiments were carried out in which the hydrophone was moved vertically and transversely, and the variation of $\overline{p^2}$ was measured. This was done for a wave slope of 0.263, and we then assumed that the factor m was constant for other values of the experimental parameters. This is a reasonable assumption because the hydrophone was located 7 m downstream of the breaking event, in the acoustic far field ($kr \gg 1$) where the properties of the waveguide would tend to dominate time-averaged quantities such as $\overline{p^2}$. As a result, the functional form of the variation of $\overline{p^2}$ across the channel would not vary as the wave slope was changed, giving a constant value for m.

In order to estimate the total acoustic energy radiated, a measure of the amount of acoustic energy radiated upstream of the event was also required. Hydrophone measurements upstream of one event, $S = 0.263$, showed that for this wave slope the same amount of energy was radiated upstream as downstream. Therefore the value of E_{a} calculated from equation (16) was multiplied by a factor of two to obtain an estimate of the total acoustic energy radiated away from the breaking region.

The wave energy dissipated is approximated by

$$E_{\mathrm{L}} = \tfrac{1}{2}\rho g C_{\mathrm{g}} b T_{\mathrm{w}} \overline{\eta_{\mathrm{d}}^2}, \tag{17}$$

where T_{w} is the sampling interval, C_{g} is the group velocity of the centre component, b is the channel width and $\overline{\eta_{\mathrm{d}}^2}$ is the surface displacement variance dissipated due to breaking (cf. equation (3)). Figure 19 shows the estimated total acoustic energy

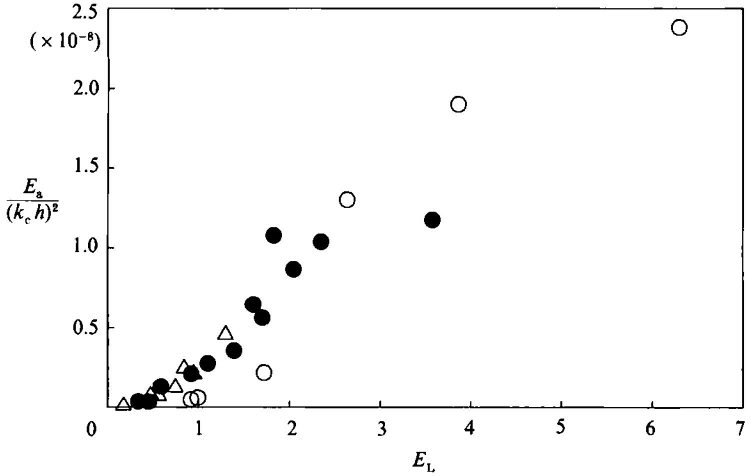

FIGURE 19. Correlation between the estimated radiated acoustic energy E_a scaled by $(k_c h)^{-2}$ and the energy dissipated by the breaking wave E_L. ○, P_1; ●, P_2; △, P_3.

radiated scaled by $(k_c h)^{-2}$ versus the energy dissipated by the breaking wave. The correlation produced by this scaling suggests that shorter breaking waves radiate more acoustic energy per unit of mechanical wave energy dissipated. The fraction of dissipated wave energy which is radiated as sound is of order 10^{-8}.

We wish to thank our colleagues at Lincoln Laboratory, MIT, for the loan of microwave equipment. This work was supported by grants from the Office of Naval Research (Physical Oceanography, Remote Sensing and Acoustic Reverberation SRP) and the National Science Foundation (8614889-OCE).

REFERENCES

ALPERS, W., ROSS, D. B. & RUFENACH, C. L. 1981 On the detectability of ocean surface wave by real and synthetic aperture radar. *J. Geophys. Res.* **86**, 6481–6498.

BANNER, M. H. & CATO, D. H. 1987 Physical mechanisms of noise generation by breaking waves – laboratory study. In *Proc. NATO Adv. Workshop on Natural Mechanisms of Surface Generated Noise in the Ocean, Lerici, Italy*, pp. 429–436.

BANNER, M. L. & FOOKS, E. H. 1985 On the microwave reflectivity of small-scale breaking water waves. *Proc. R. Soc. Lond.* A **399**, 93–109.

BENDAT, J. S. & PIERSOL, A. G. 1986 *Random Data, Analysis and Measurement Procedures*, 2nd Edn. Wiley-Interscience.

BREKHOVSKIKH, L. & LYSANOV, YU. 1982 *Fundamentals of Ocean Acoustics*. Springer.

CROWTHER, P. A. 1987 Bubble noise creation mechanisms. In *Proc. NATO Adv. Workshop on Natural Mechanisms of Surface Generated Noise in the Ocean, Lerici, Italy*, pp. 131–150.

CROWTHER, P. A. 1989 Some statistics of sea noise. *J. Acoust. Soc. Am.* **85**, suppl. 1, 117th meeting of ASA, Syracuse NY (abstract).

EWELL, G. W., TULEY, M. T. & HORNE, W. F. 1984 Temporal and spatial behavior of high resolution sea clutter 'spikes'. *IEEE Radar 84 Conf.*, pp. 100–104.

FARMER, D. M. & VAGLE, S. 1987 Observations of high frequency ambient sound generated by the wind. In *Proc. NATO Adv. Workshop on Natural Mechanisms of Surface Generated Noise in the Ocean, Lerici, Italy*, pp. 403–416.

FARMER, D. M. & VAGLE, S. 1988 On the determination of breaking wave distributions using ambient sound. *J. Geoph. Res.* **93**, 3591–3600.

Jessup, A. T., Keller, W. C. & Melville, W. K. 1990 Measurements of sea spikes in microwave backscatter at moderate incidence angles. *J. Geophys. Res.* **95**, 9679–9688.

Keller, W. C., Plant, W. J. & Valenzuela, G. R. 1981 Observations of breaking ocean waves with coherent microwave radar. In *IUCRM Symposium on Wave Dynamics and Radio Probing of the Ocean Surface, Miami Beach, Fl.* (Also in *Wave Dynamics and Radio Probing of the Sea Surface* (ed. O. M. Phillips & K. Hasselmann). Plenum, 1986.)

Kerman, B. R. 1984 Underwater sound generation by breaking wind waves. *J. Acoust. Soc. Am.* **75**, 149–165.

Kwoh, D. S. & Lake, B. M. 1981 Microwave backscatter from short gravity waves: deterministic, coherent, dual-polarized study of the relationship between backscatter and water wave properties. In *IUCRM Symposium on Wave Dynamics and Radio Probing of the Ocean Surface, Miami Beach, Fl.* (Also in *Wave Dynamics and Radio Probing of the Sea Surface* (ed. O. M. Phillips & K. Hasselmann). Plenum, 1986; see also similar title in *IEEE J. Ocean. Engng* OE-**9**, 291–308, 1984.)

Longuet-Higgins, M. S. 1989 Monopole emission of sound by asymmetric bubbles oscillation. Part 1. Normal modes. *J. Fluid Mech.* **201**, 525–541.

Longuet-Higgins, M. S. & Smith, N. D. 1983 Measurements of breaking waves by a surface jump meter. *J. Geophys. Res.* **88**, 9823–9831.

Medwin, H. 1989 Bubble sources of the Knudsen sea noise spectra. *J. Acoust. Soc. Am.* **86**, 1124–1130.

Medwin, H. & Daniel, A. C. 1990 Acoustical measurements of bubble production by spilling breakers. *J. Acoust. Soc. Am.* **88**, 408–412.

Melville, W. K., Loewen, M. R., Felizardo, F. C., Jessup, A. T. & Buckingham, M. J. 1988 Acoustic and microwave signatures of breaking waves. *Nature* **336**, 54–59.

Melville, W. K. & Rapp, R. J. 1985 Momentum flux in breaking waves. *Nature* **317**, 514–516.

Monahan, E. C. & O'Muirheartaigh, I. G. 1986 Whitecaps and the passive remote sensing of the ocean surface. *Intl J. Remote Sensing* **7**, 627–642.

Phillips, O. M. 1988 Radar returns from the sea surface – Bragg scattering and breaking waves. *J. Phys. Oceanogr.* **18**, 1065–1074.

Prosperetti, A. 1987 Bubble dynamics in oceanic ambient noise. In *Proc. NATO Adv. Workshop on Natural Mechanisms of Surface Generated Noise in the Ocean, Lerici, Italy*, pp. 151–171.

Rapp, R. J. 1986 Laboratory measurements of deep water breaking waves. Ph.D. thesis, Ocean Engineering, Massachusetts Institute of Technology.

Rapp, R. J. & Melville, W. K. 1990 Laboratory measurements of deep water breaking waves. *Phil. Trans. R. Soc. Lond.* A **331**, 735–800.

Ulaby, F. T., Moore, R. K. & Fung, A. K. 1982 *Microwave Remote Sensing Active and Passive*, Vol. II. Addison-Wesley.

Wu, J. 1979 Oceanic whitecaps and sea state. *J. Phys. Oceanogr.* **9**, 1064–1068.